

1 3-D Q-coda attenuation structure at Mt. Etna

2 (Italy)

3 E. Giampiccolo<sup>1</sup>, E. Del Pezzo<sup>2,3</sup>, T. Tuvé<sup>1</sup>, G. Di Grazia<sup>1</sup>  
and J. M. Ibáñez<sup>1,3</sup>

4 April 8, 2021

5 (1) INGV - Osservatorio Etneo, Piazza Roma 2, Catania, Italy.

6 (2) INGV - Osservatorio Vesuviano, via Diocleziano 328, Napoli, Italy.

7 (3) Instituto Andaluz de Geofísica, Universidad de Granada, Spain.

8 **Abstract**

9 Three dimensional attenuation pictures of Mt. Etna volcano ob-  
10 tained by the analysis of Q-coda from local volcano-tectonic earth-  
11 quakes are presented in this work. Seismic sources are confined inside  
12 the Etna structure with a maximum focal depth of 35 km below the sea  
13 level. The space distribution of the attenuation values was calculated  
14 by using 3-D weighting functions derived by the sensitivity kernels of  
15 Pacheco and Snieders and approximated by a polynomial interpola-  
16 tion, represented in the maps by using a back- projection method.  
17 Data were analyzed in four bands with central frequency placed at 1.5,  
18 3, 6 and 12 Hz respectively. We observed a frequency dependence of  
19 Q-coda with values that range from 55 at 1.5 Hz to 218 at 12 Hz.

20 Q-coda space distribution in the Etna area shows almost uniformity  
21 in the average attenuation in the first 35 km below the surface. The  
22 images were derived with a resolution of 5 km. We observe as one  
23 of our main conclusions that Q-coda attenuation space anomalies are  
24 correlated with the areas of highest structural heterogeneities and are  
25 distributed along the well-known tectonic structures which characterize  
26 the crust in Mt. Etna region. Previous and numerous velocity and  
27 attenuation images describing the structure of Mt. Etna support our  
28 main conclusion: high Q-coda volumes almost coincide with the zones  
29 marked by high velocity and relative low total attenuation for direct  
30 waves.

31 Keywords: Etna volcano, Seismic Imaging, Coda waves, Q-coda

## 32 1 Introduction

33 The investigation of the crust and upper mantle structure of Mt. Etna vol-  
34 cano has been a big challenge for the volcanological community since many  
35 decades ago (Cassinis et al., 1969; Sharp et al., 1980; Hirn et al., 1991; Car-  
36 daci et al., 1993; Hirn et al., 1997). From the year 2000 up to the present,  
37 seismological studies, accompanied by the progressive enhancement in in-  
38 struments and methods, contributed with new observations and models to  
39 improve the knowledge of the geological structure of this volcanic region. For  
40 instance, tomographic studies provided new 3D velocity images of this area  
41 improving number and quality of the structural models (Chiarabba et al.,  
42 2000; Laigle et al., 2000; Patanè et al., 2002 ; Aloisi et al., 2002; Chiarabba  
43 et al., 2004; Patanè et al., 2006; De Gori et al., 2011; Alparone et al., 2012;

44 Díaz-Moreno et al., 2018; Giampiccolo et al., 2020). All these works provided  
45 an increasing number of details showing low- and high-velocity anomalies  
46 depicting lateral discontinuities and evidencing the structural complexity of  
47 this volcanic area.

48 Since the attenuation of P- and S-waves provides important additional  
49 information on the Earth structure, because of its sensitivity to rock com-  
50 position, fluid content, temperature and other properties, it turns out that  
51 it is a necessary information to complement the velocity imaging. The at-  
52 tenuation images permit in facts a more complete structural interpretation  
53 and become crucial in volcanoes, where high temperature, hot fluids, par-  
54 tial melting and heterogeneity of the geological structures strongly affect the  
55 rock properties.

56 It is well known that the attenuation mechanism depends on one hand by  
57 the existence of significant heterogeneity, on the other hand by the presence  
58 of molten materials as magma lens or bodies. This leads to a wide variety of  
59 examples that associate different volcanic structures (rigid, cooled, molten)  
60 with geological conditions. (e.g. Del Pezzo, 2008; Sato et al., 2012). In this  
61 sense, Mt. Etna volcano is the ideal scenario to perform studies on attenu-  
62 ation imaging (Martinez-Arevalo et al., 2005; De Gori et al., 2005; De Gori  
63 et al., 2011; Alparone et al., 2012; Ibáñez et al., 2020). It is noteworthy  
64 that all the above mentioned works have evidenced the absence of a clear  
65 high attenuation anomaly in the crust that could be interpretable as melt  
66 accumulation and therefore as a possible magma chamber in the crust. Con-  
67 versely, the combination of velocity and attenuation studies has evidenced  
68 the existence of strong lateral anomalies interpreted as a broad complex of

69 intrusive bodies, placed in the middle and upper crust, that explain the  
70 feeding mechanism of the volcanic system. (e.g. Patanè et al., 2011).

71 Mt. Etna is an ideal scenario to develop any type of tomographic stud-  
72 ies thanks to the large local earthquake data set available. Since the local  
73 earthquakes beneath the volcano (Figure 1) occurring in such heterogeneous  
74 medium generate high Energy diffusive- (or scattering-) wave fields (the coda  
75 waves), Scattering Tomography is easily applicable. The images produced  
76 using this approach reveal to be complementary to the already obtained to-  
77 mography images in velocity and attenuation, both for P- and S- waves (see  
78 e.g. Larose et al., 2010 and references therein). Among the different methods  
79 based on the analysis of the diffusive wave field, the Coda wave interferome-  
80 try (Snieder, 2004) is used to individuate single elastic anomalies in the earth  
81 medium, while the coda waves imaging (Mayor et al., 2016; Prudencio et al.,  
82 13 a) yields pictures of the attenuation space distribution. Crucial in these  
83 last approaches is the use of the Sensitivity Kernels of the scattering wave  
84 field. Their estimation is based on the “Average Local Time”, concept that is  
85 defined as the time in which the Elastic Wave Energy pass through a small  
86 volume of Earth located at a given space position (Obermann et al., 2013).  
87 The Sensitivity Kernels are thus space-time functions describing the space-  
88 time distribution of seismic energy. They, in other words, describe where and  
89 when in the earth medium the seismic radiation composing the coda of the  
90 local earthquakes is generated. For this reason the Sensitivity Kernels are  
91 extremely important to associate the attenuation parameter(s) derived by  
92 the analysis of seismic coda with a particular zone inside the earth medium,  
93 allowing the construction of an attenuation image. Recently, Sensitivity Ker-

94 nels for scattering radiation have been used to depict 2D and 3D volcanic  
95 structures (see for example the works of De Siena et al., 2013, Prudencio  
96 et al. 13 a, Prudencio et al., 13 b, Prudencio et al., 2015, Del Pezzo et al.  
97 2016, De Siena et al., 2016) or to study tectonically active zones (e.g. Mayor  
98 et al., 2016, Sketsiou et al., 2020). In the present paper we obtained a 3D  
99 Q-coda tomography for Mt. Etna using a projection method based on the  
100 use of weighting functions derived from the Sensitivity Kernels calculated by  
101 Pacheco and Snieder (2006), and compared the results obtained with some  
102 of the previous seismological (mainly in velocity) images of this volcano. In  
103 addition, we studied the correspondence of the present results with a recent  
104 2D structure of the shallow part of Etna based on the joint measurements of  
105 intrinsic- and scattering-attenuation (Ibáñez et al., 2020), carried out using  
106 passive and active data sets. The present Q-coda tomography reproduces  
107 the S-wave attenuation structure for this volcano down to a depth of 35 km  
108 in four frequency bands centered at 1.5, 3, 6 and 12 Hz respectively. We  
109 will show how our present images evidence that the strongest attenuation  
110 contrasts are well correlated with the local geotectonic setting, and with the  
111 pattern of the main faults and fractures characterizing the crust at Mt. Etna.  
112 In addition, the observed correspondence of the present results with those  
113 from previous studies confirms the goodness and success of the technique  
114 as a complementary tool to be combined with the well-known tomographic  
115 images in velocity.

## 116 **2 Structural and seismological setting of the Mt.** 117 **Etna area**

118 Mt. Etna volcano (Figure 1) is one of the best European volcanic laborato-  
119 ries and its associated natural seismicity is ideal to study the deep structure  
120 beneath an active volcano. It is a 3300 m high polygenetic volcano, placed on  
121 the eastern coast of Sicily in front of the Apennine-Maghrebian collision belt  
122 (Lentini, 1982). In the literature is possible to find several works that de-  
123 scribe many structural aspects of the volcanic environment (De Guidi et al.,  
124 2014). However, the complex tectonic and geodynamic setting is still under  
125 study, with a broad set of hypotheses interpreting its origin and evolution  
126 (i.e. Rittmann, 1973; Continisio et al., 1997; Hirn et al., 1997; Tanguy et al.,  
127 1997; Gvirtzman and Nur, 1999; Faccenna et al., 2001; Clocchiatti et al.,  
128 2004). The the N-S compression, active in northern Sicily, dominates the  
129 regional deformation (Bousquet and Lanzafame, 2004) that is contempora-  
130 neously active with an E-W extension, active on the eastern side, and with  
131 a right-lateral transtension both offshore along the Malta Escarpment Fault  
132 System (MEFS; Figure1) and onshore along the Timpe Fault System (TFS;  
133 Figure 1) and with set of parallel normal faults striking from NNW to NW  
134 (Azzaro et al., 2012). In particular, the important zones of Valle del Bove  
135 (VdB) and the volcano-tectonic structures of the NE Rift (Figure 1) placed in  
136 the eastern flank of the volcano are separated from the Ioanian Coast by the  
137 Pernicana Fault (PF) and by the Timpe Fault System, which are considered  
138 the most important tectonic elements at Mt. Etna (see Azzaro et al. 2012Az-  
139 zaro et al. 2013Azzaro et al. 2017) controlling the ESE seaward displacement

140 of the eastern flank as indicated by numerous studies (e.g. Borgia et al. 1992;  
141 Lo Giudice et al. 1992; Rust and Neri 1996; Bonforte and Puglisi 2003; Rust  
142 et al. 2005; Branca and Ferrara 2013; Urlaub et al. 2018 among others). The  
143 seismicity of Mt. Etna is mainly characterized by crustal shallow ( $<10$  km  
144 depth) volcano-tectonic earthquakes (VT), related to the seismic activity of  
145 the already described fault systems and to the volcano induced stress dy-  
146 namics generating seismic activity (e.g. Patanè et al., 2004; Solaro et al.,  
147 2010). The most intense seismic activity occurs in the eastern flank of the  
148 volcano, associated with the Timpe Fault System and the Pernicana Fault.  
149 The latter fault system is composed by few active tectonic structures mainly  
150 aligned with the E-W direction, showing a peculiar seismic pattern, as ev-  
151 idenced by the above cited authors. Other structures are the N-S trending  
152 Ragalna Fault System (RFS) and the NW–SE Trecastagni and Tremestieri  
153 faults (TCF; TMF) in the South (Azzaro et al., 2013 and references therein;  
154 Alparone et al., 2013). These structures generate frequent moderate mag-  
155 nitude earthquakes which historically caused destruction or severe damage  
156 in the villages and cities of the area. Intermediate ( $10 < h < 15$  km) and deep  
157 ( $15 < h < 35$  km) earthquakes, occurring beneath the western flank of the vol-  
158 cano (Figure 1) in some cases have been associated with episodic movements  
159 of magmatic batches from depth toward the surface (e.g., Musumeci et al.,  
160 2004; Alparone et al., 2012; Mostaccio et al., 2013). In the deep crust (be-  
161 tween 22 and 30 km of depth) beneath the north-western area of Mt. Etna  
162 volcano is placed one of the most significant deep seismo-genic volumes (Az-  
163 zaro et al., 2017). However, this seismicity is at the present interpreted  
164 on the base of tectonic regional dynamics associated with the well-known

165 compressive regime at the front of the Sicilian Chain-Foreland (Lavecchia  
166 et al., 2007; Scarfi et al., 2016). In addition, local VT seismicity associ-  
167 ated with deformation processes (inflation-deflation) of the volcanic edifice,  
168 ground fracturing due to magma injection in shallow dike systems and other  
169 processes related to the Mt. Etna dynamics are observed in the summit  
170 region. Other sources of deformation in the Mt. Etna edifice are associated  
171 with the morphological conditions related to flank gravitational instability  
172 or to regional normal-oblique faulting (Azzaro et al., 2013). Finally, impor-  
173 tant is also the presence of underground water reservoir beneath Mt. Etna  
174 to understand the observed seismic behavior. Federico et al. (2017) show  
175 that Mt. Etna is characterized by discontinuous low-permeability pyroclas-  
176 tic layers interbedded in highly permeable lavas. The additional existence  
177 in the region of an impermeable substratum creates an important ground-  
178 water reservoir beneath Mt. Etna structure. The impermeable sedimentary  
179 basement morphology controls the confined deep water circulation. Since  
180 the basement of Mt. Etna has its highest elevation (about 1300 m a.s.l.),  
181 placed a few kilometres towards northwest of the volcano summit and dip-  
182 ping toward the southeast, groundwater tends to move and accumulate in  
183 the eastern and southern flanks of the volcano (Ogniben 1966; Branca and  
184 Ferrara 2013)

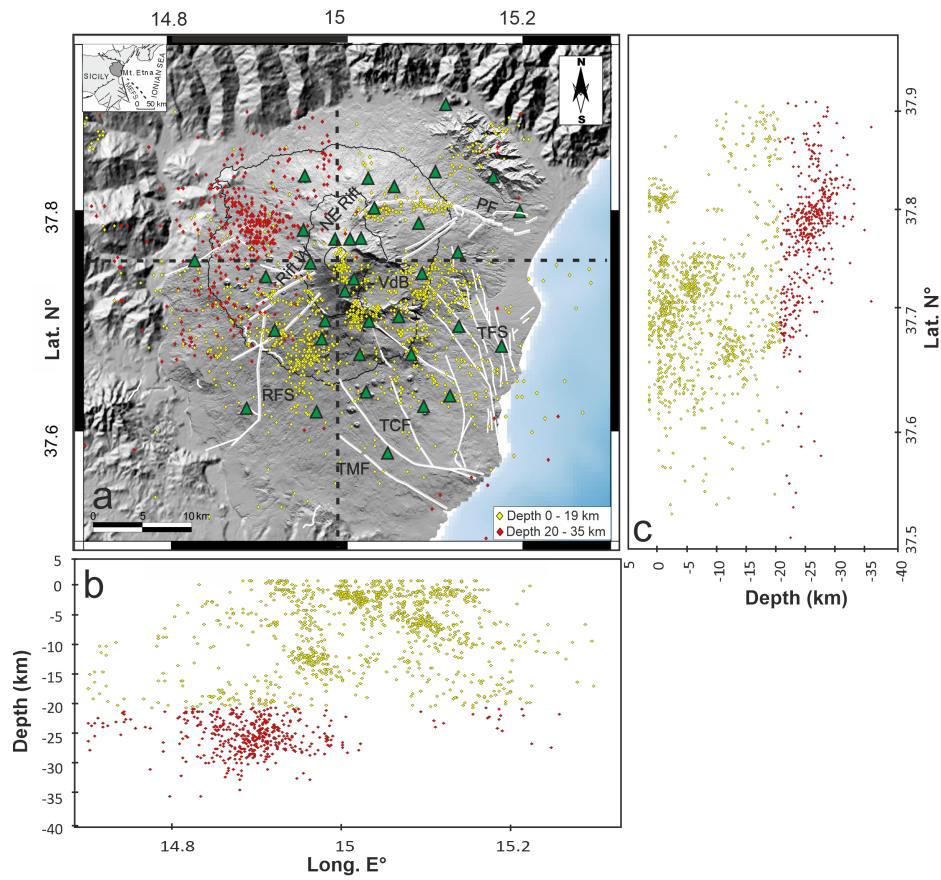


Figure 1: Map of the Etna area. Green triangles represents the receiver locations. Red dots mark the deepest, (upper mantle), while yellow dots the shallowest (crust) earthquake sources. White lines depict the Etna faults. Black dotted lines are the profiles of cross sections shown in figure 6. In the inset, dashed lines depict the regional fault structures. b) Hypocenters projected in a E-W section. c) Hypocenters projected in a N-S section.

## 185 3 Theory, Methods and Data Processing

### 186 3.1 Q-coda

187 It is well known that the total-Q or  $Q_t$ , the total quality factor for seismic  
188 waves, can be expressed as

$$Q_i^{-1} + Q_s^{-1} = Q_t^{-1}$$

189 where  $Q_i$  is the intrinsic-Q, accounting for the Energy transformed in heat  
190 during the propagation, and  $Q_s$  is the scattering-Q, accounting for the pri-  
191 mary wave Energy lost by scattering from the medium heterogeneities and  
192 recovered in the seismic coda of the local earthquakes.

193 Q-coda, hereafter  $Q_c$ , is the parameter describing the time decay of the  
194 Seismogram Coda Energy Envelope. Assuming 3D body wave propagation  
195 in a half space with constant velocity

$$E(\omega, t) \propto \frac{E_0}{t^2} \exp\left(-\frac{\omega t}{Q_c}\right) \quad (1)$$

196 where  $E(\omega, t)$  represents the short period local or regional seismogram En-  
197 ergy Envelope,  $E_0$  is the source Energy,  $\omega$  is the angular frequency,  $t$  is  
198 the time elapsed since the origin time of the earthquake. Aki and Chouet  
199 (1975) showed that equation (1) corresponds to the Single Scattering model  
200 in case of co-located source and receiver, and interpreted  $Q_c$  as the total-Q  
201 for S-waves. Since the appearance in literature of this pioneering paper, a  
202 large number of Q-coda estimates were carried out in the world, with the  
203 main purpose of estimating  $Q_t$ . Sato (1977) introduced the source-receiver

204 distance,  $r$ , and reformulated the Single-scattering model as

$$E(\omega, r, t) = \frac{E_0 g_0}{4\pi r^2} K\left(\frac{vt}{r}\right) H(vt - r) \exp\left(-\frac{\omega t}{Q_c}\right) \quad (2)$$

205 where  $g_0$  is called "scattering coefficient", the inverse of the mean free path,  
206  $l_0$ ,  $v$  is the S-wave speed,  $H$  represents the Heaviside function and  $K(x) =$   
207  $\frac{1}{x} \ln\left(\frac{x+1}{x-1}\right)$ .

208 It was later demonstrated (Zeng et al., 1991) that the equation (2) is the  
209 first order approximation, strictly valid only for large  $l_0$ , of the 3D solution  
210 of the general Energy Transport integral equation. A solution of this last  
211 equation, accounting for multiple scattering, was found by Paasschens (1997)  
212 with an interpolation procedure. Unfortunately, the conditions for the appli-  
213 cation of the single scattering assumption in the real Earth are far from being  
214 realistic, and in most experimental works the estimate of attenuation carried  
215 out measuring  $Q_c$  is biased due to the underlying assumption of half space  
216 with constant velocity. In such studies it emerges that  $Q_c$ , for most of the  
217 study areas, is a measure of  $Q_i$  and not of  $Q_t$  for S-waves, as was assumed in  
218 the early applications, and that the absolute value of  $Q$  is generally underes-  
219 timated due to the unrealistic assumption of half space. This clearly emerges  
220 from attenuation studies based on the so called MLTWA technique (see e.g.  
221 Mayeda et al., 1992 and Sato et al., 2012 or Del Pezzo and Ibañez, 2020 for a  
222 review) and successive studies which resolve the trade-off between  $Q_i$  and  $Q_s$   
223 by integrating the energy associated with the ballistic waves (Gaebler et al.,  
224 2015; Eulenfeld and Wegler, 2017; Eulenfeld and Wegler, 2016). In these  
225 studies, the solution of the general Transport Equation (see e.g. Margerin,

226 2011 for a review) is applied to jointly retrieve  $Q_i$  and  $Q_s$ . The measure  
227 of  $Q_c$  has been found to depend on the time interval selected for coda anal-  
228 ysis, generally taken starting the analysis at twice the S-wave travel time  
229 and ending at 60 - 100s after the origin time, depending on the earthquake  
230 magnitude and experimental conditions (Sato et al., 2012). This happens  
231 due to the improper application of equation (2) to the cases where the single  
232 scattering approximation is unrealistic. In such cases, when the maximum  
233 lapse time is closer to the S-wave travel time, the single scattering phenom-  
234 ena prevail in the coda composition, and  $Q_c$  is closer to  $Q_t$ ; at longer time  
235 intervals the coda waves begin to be enriched by multiply scattered waves,  
236 and in this case  $Q_c$  approaches  $Q_i$  (Mayor et al., 2016). In synthesis, in the  
237 range of the coda time intervals above indicated, for increasing  $l_0$   $Q_c$  tends  
238 to  $Q_i$ , while in earth media characterized by strong heterogeneity (short  $l_0$ ),  
239  $Q_c$  depends also on the degree of heterogeneity, and is closer to  $Q_t$  than to  $Q_i$   
240 (Del Pezzo and Ibañez, 2020). From the above discussion it emerges that  $Q_c$   
241 cannot be seen as a rock attribute as its relation with the elastic property of  
242 the rocks is unclear, rather a coefficient describing the energy propagation.

243 The reason why  $Q_c$ , and not the couple  $Q_i$  and  $Q_s$ , is still used worldwide  
244 to characterize the space distribution of the seismic attenuation, is that in the  
245 fit of the general Energy Transport Equation with the (single-path) observed  
246 Seismogram Energy Envelope, there is a strong trade-off between  $Q_i$  and  $Q_s$ .

### 247 **3.2 The weighting functions for Q-coda imaging**

248 The first Q-coda image (2D) was obtained by Singh and Herrmann (1983).  
249 These authors assigned the single  $Q_c$  values to the middle point of the seg-

250 ment connecting source and receiver, and then composed the image using  
251 spatial smoothing. Xie and Mitchell (1990) described a back-projection  
252 procedure, based on assigning the measured  $Q_c$  values to any point (with  
253 the same probability) in the whole scattering ellipse, which was used as a  
254 very simplified weighting function. More recently, Calvet et al. (2013) and  
255 De Siena et al. (2016) jointly used  $Q_c$  and the S-wave envelope peak delay  
256 (proportional to  $Q_s$ ) as observables to draw a 2D picture of attenuation re-  
257 spectively in Pyrhenees and Saint Helens volcano. In the imaging procedure  
258 Calvet et al. (2013) still use a very simplified weighting function for Q-coda,  
259 similar to that described by Xie and Mitchell (1990), while De Siena et al.  
260 (2016) use a weighting function similar to that in the present paper.

261 In the present paper we use the approach described by Del Pezzo et al.  
262 (2018) to calculate a polynomial approximation of the sensitivity kernel for  
263 Q-coda discussed by Pacheco and Snieder (2006), which we use in the present  
264 approach as weighting functions, heuristically giving them a probabilistic  
265 meaning. Detailed studies on sensitivity kernels for the scattering radiation  
266 can be found in Pacheco and Snieder (2006), Obermann et al. (2013) Planès  
267 et al. (2014), Mayor et al. (2014), Margerin et al. (2016) and Zhang et al.  
268 (2021). The polynomial approximation of the sensitivity kernel for Q-coda  
269 is given by the equation described in Appendix 1. In Figure 2 we show a  
270 contour plot example of its space pattern.

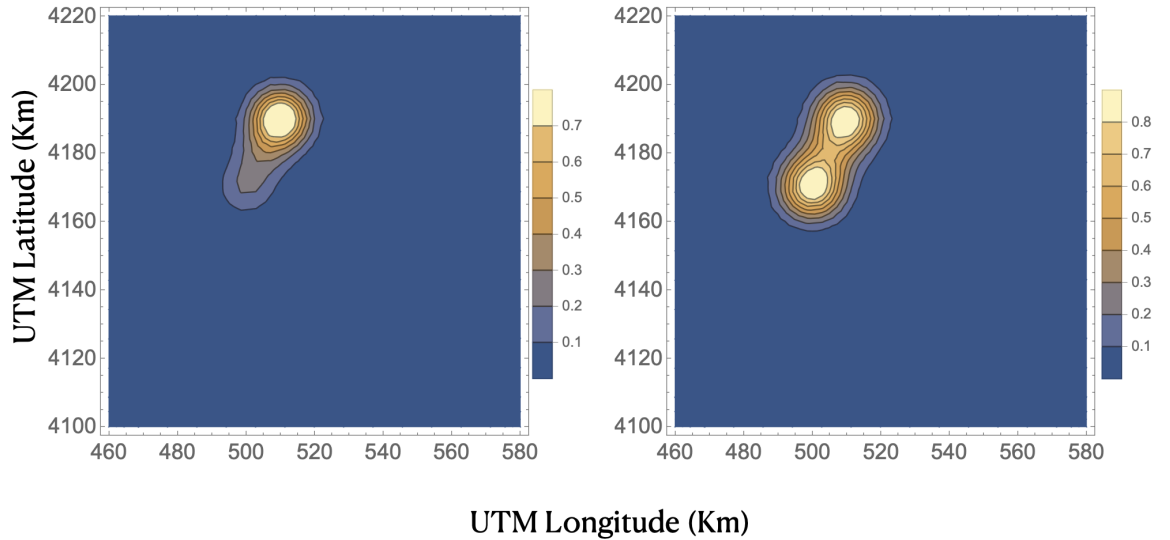


Figure 2: Left panel: Isolines of function  $w$  calculated fixing the depth at 0.1 km for a source located at UTM Longitude 500.0, UTM Latitude 4170.0, Depth 10.0 km, and a receiver at UTM Longitude 510.0, UTM Latitude 4190.0, located at surface. Right Panel: Isolines for a source located at the same epicenter as in the left panel, at a depth of 0.0 km, with receiver in the same position.

### 271 3.3 The method of imaging

272 The method used in the present paper to construct the images is described  
 273 in detail in Del Pezzo and Ibañez (2020). Here only a brief outline will be  
 274 given. The method consists in estimating  $\bar{q}_i$ , the estimate of  $Q_c$  for the  $i$ -th

275 source-receiver couple, where  $i$  spans over all the  $N$  couples. The volume  
 276 under study is divided in cells.  $\bar{q}_i$  is then assigned to the  $j - th$  space cell,  
 277 weighted by the weighting function correspondent to the the  $i - th$  couple,  
 278  $w(x_j, y_j, z_j, r_i, t_l, v)$ , here denoted as  $w_{ij}$ .  $w_{ij}$  represents the probability that,  
 279 for the  $i$ -th source-receiver couple positioned respectively at  $\{x_{si}, y_{si}, z_{si}\}$  and  
 280  $\{x_{ri}, y_{ri}\}$ , the product  $\bar{q}_i w(x_j, y_j, z_j, r_i, t_l, v)$  (see Appendix 1 for the analytic  
 281 expression of the function  $w$ ) is calculated for any couple (index  $i$ ) and in  
 282 the center of any cell (index  $j$ ), and will be indicated for simplicity  $\bar{q}_i w_{ij}$ .  $r_i$   
 283 indicates the distance between the source and receiver and  $t_l$  the maximum  
 284 lapse time.

285 The best estimator of  $Q_c$  in the  $j - th$  cell,  $Q_{cj}$ , will be given by

$$Q_{cj} = \frac{\sum_i \bar{q}_i w_{ij}}{\sum_i w_{ij}} \quad (3)$$

### 286 3.4 Data analysis

287 For the present work we used 1600 earthquakes with magnitudes placed in  
 288 the interval  $2.0 < ML < 4.5$  located in Mt. Etna edifice for the time interval  
 289 of 2006–2019 and recorded by the permanent seismic network of the Istituto  
 290 Nazionale di Geofisica e Vulcanologia-Osservatorio Etneo (INGV-OE). All  
 291 the seismic stations used for the present analysis were equipped with three-  
 292 component, broadband (0.01–40 s period), 24-bit resolution seismometers,  
 293 digitizing the signals at 100 samples per second. The data set including P-  
 294 and S-wave arrival times, location parameters and raw seismic waveforms,  
 295 were downloaded from the INGV-OE data base and catalogue (Alparone  
 296 et al., 2015 and Alparone et al. 2020).

297 The selection of the data set was done on the base of the best located  
298 earthquakes, fulfilling the constraints of having at least 6 P- and 2 S-arrival  
299 times, a root mean squared travel time residual, RMS, lower than 1s, az-  
300 imuthal gap smaller than 180 degrees and hypocentral errors smaller than  
301 1.0 km. A final set of 5695 three component seismograms was used for the  
302 coda-Q analysis.

303  $\bar{q}_i$ , the estimate of  $Q_c$  for the  $i$ -th source receiver couple, was estimated  
304 using the following procedure. First, we estimated the Energy Envelope of  
305 the seismogram for the two horizontal components selecting for the analysis  
306 the signal starting at twice the S-wave travel time and ending at 30 seconds  
307 from the origin time. We calculated the Energy spectra of 3 s long time win-  
308 dows, sliding along the seismogram 1.5 s each step. For each spectrum the  
309 Energy averaged in four successive frequency bands, centered respectively at  
310  $f_c = 1.5, 3.0, 6.0$  and  $12.0$  Hz with a bandwidth in the interval between  $f_c/2$   
311 and  $2f_c$  was estimated. The value of this average for each spectrum was  
312 attributed to the center of the time interval, finally obtaining the Energy-  
313 time Envelope. This approach is parallel to the ordinary method used first  
314 by (Aki and Chouet, 1975) where envelopes were estimated by filtering in  
315 separate frequency bands (see e.g. Giampiccolo and Tuvè, 2018). The Par-  
316 seval theorem ensures that in wide hypotheses, RMS of the filtered trace is  
317 equivalent to the integral of Fourier spectrum in the same frequency band  
318 used for filtering.

319 The Envelopes then were Log-averaged over the two horizontal compo-  
320 nents, and eventually  $\bar{q}_i$  was estimated fitting the Log-averaged Envelope  
321 to Equation (2).  $\bar{q}_i$  values with an uncertainty higher than 100% of their

322 value, were rejected. The vertical component was excluded due to its lower  
 323 signal-to-noise ratio at the end of the coda, in comparison with the hor-  
 324 izontal components. However, it was tested that this exclusion does not  
 325 significantly change the Q-coda estimates. Figure 3 shows an example seis-  
 326 mogram (3 components) together with the spectra of the first time window,  
 327 starting at twice the S-wave travel time and the last one in the late coda,  
 328 starting at 27 seconds after the origin time.

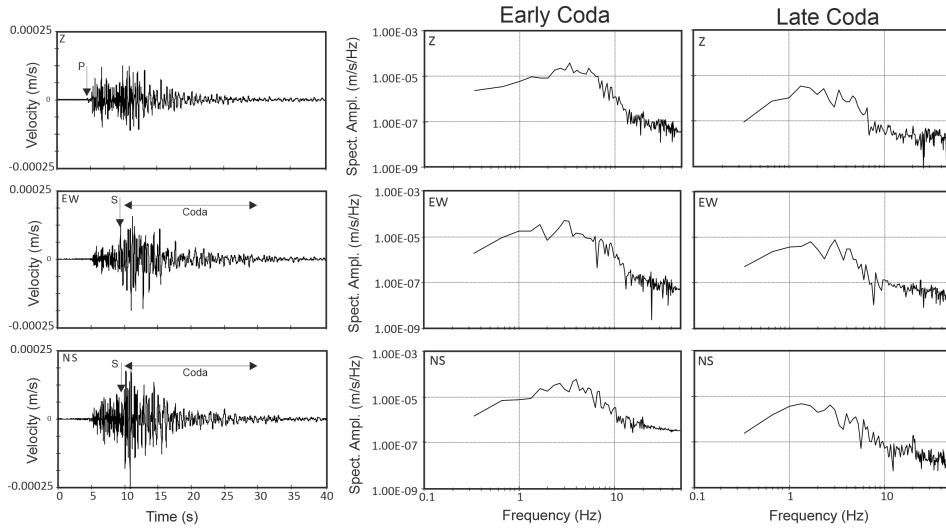


Figure 3: An example of seismograms (leftmost panels) for a shallow ( $h=4$  km)  $ML=3.4$  earthquake recorded at ECTS station (epicentral distance = 25 km). From top to bottom Vertical (Z), East–West (EW), North–South (NS) components are shown. On the rightmost panels, the amplitude spectra calculated in the early and late coda windows, respectively, for all components.

### 329 3.5 Results

330 The average of  $\bar{q}_i$  (over the  $N$  source-receiver couples),  $\langle \bar{q}_i \rangle_N$ , is reported  
 331 in Table 1.

Table 1  
Q-coda averaged over the source-receiver couples for the four frequency  
bands utilized.

All depths (N=5935)

Frequency (Hz)	$\langle \bar{q}_i \rangle_N$	$\sigma_q$
1.5	55.0	0.3
3.0	80.4	0.3
6.0	112.1	0.4
12.0	213.4	0.4

Crustal earthquakes (N=4815)

Frequency (Hz)	$\langle \bar{q}_i \rangle_N$	$\sigma_q$
1.5	54.1	0.4
3.0	79.9	0.4
6.0	111.7	0.4
12.0	216.9	0.4

Mantle earthquakes (N=1120)

Frequency (Hz)	$\langle \bar{q}_i \rangle_N$	$\sigma_q$
1.5	55.6	0.8
3.0	82.4	0.8
6.0	114.1	0.8
12.0	198.5	0.8

332 In the same Table we provide the averages  $\langle \bar{q}_i \rangle_N$  estimated for two  
333 focal depth ranges: a) ranging between surface and 18 km (crustal earth-  
334 quakes); b) ranging from 18 to 35 km (upper mantle earthquakes). It is  
335 remarkable that  $\langle \bar{q}_i \rangle_N$  for crustal and upper mantle earthquakes are co-  
336 incident inside the uncertainties at all frequencies.

337 According to this observation we can assume that the attenuation effects  
338 in the upper part of lithosphere beneath Mt. Etna show no variation with  
339 depth. This assumption is complemented by a previous attenuation study  
340 (Ibáñez et al., 2020) in the same area, carried out with the objective to  
341 separately obtain the contribution of intrinsic and scattering attenuation

342 parameters in the upper part of the crust. Ibáñez et al. (2020), using active  
343 data, measured  $Q_i$  and  $Q_s$  in the shallowest part of the crust, showing that  
344  $Q_i$  spans from 34 in the frequency band centered at 4Hz, to 200 at 20Hz,  
345 while  $Q_s$  spans respectively from 10 to 50. These values indicate that in the  
346 first 2-3 km below the surface scattering phenomena prevail on the intrinsic  
347 dissipation, for the whole frequency band analyzed.

348 Using a passive data set in a depth range compared to that of the present  
349 study with a number of events smaller than the present one, Del Pezzo  
350 et al. (2015) and Del Pezzo et al. (2019) show that space averaged scattering  
351 attenuation prevails over intrinsic attenuation at low frequency, while  $Q_i$  and  
352  $Q_s$  are comparable at higher frequency. Comparing the results reported in  
353 these last two papers with the  $Q_c$  values estimated in the present paper, it  
354 results that  $Q_c$  is very close to  $Q_s$  at 1.5 Hz; is comparable with  $Q_t$  between 3  
355 and 6 Hz and approaches  $Q_i$  at high frequency (12 Hz). Preliminary results  
356 from a new attenuation study, which will be submitted soon for publication  
357 (Giampiccolo et al., in preparation), based on a revised MLTWA method  
358 applied to the present data set, confirms these previous results.

359 The images showing the space distribution of  $Q_c$  were obtained using  
360 the method described in Subsection 3.3. We considered the planes at 0, 5,  
361 10, 15, 20, 25, 30 and 35 km, normal to the depth axis. Each plane was  
362 divided in squares with side of 5km, and in the middle of the j-th square we  
363 calculated  $\bar{q}_j$  using equation (3). The complete images shown in Figures 4  
364 and 5 were eventually obtained using the graphical interpolation routines of  
365 *Mathematica*<sup>TM</sup>. North-South and East-West vertical sections are reported  
366 in Figure 6, showing the  $Q_c$  depth variation.

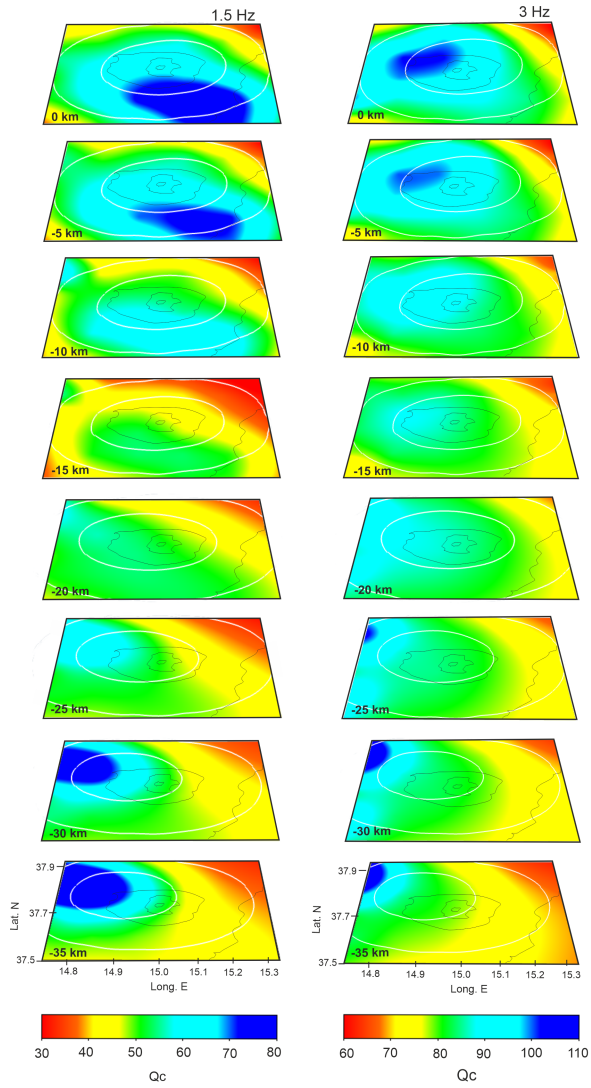


Figure 4: Slices of the 3D Q-coda image cut from 0 to 35 km depth for the first 2 frequency bands analyzed (1.5 and 3 Hz).

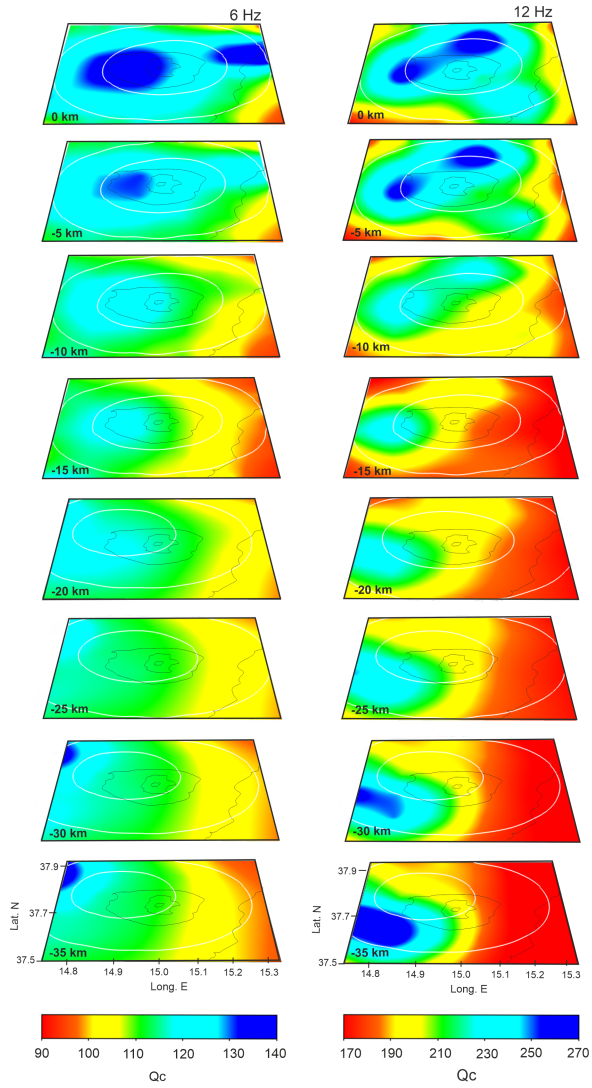


Figure 5: Slices of the 3D Q-coda image cut from 0 to 35 km depth for the last 2 frequency bands analyzed (6 and 12Hz).

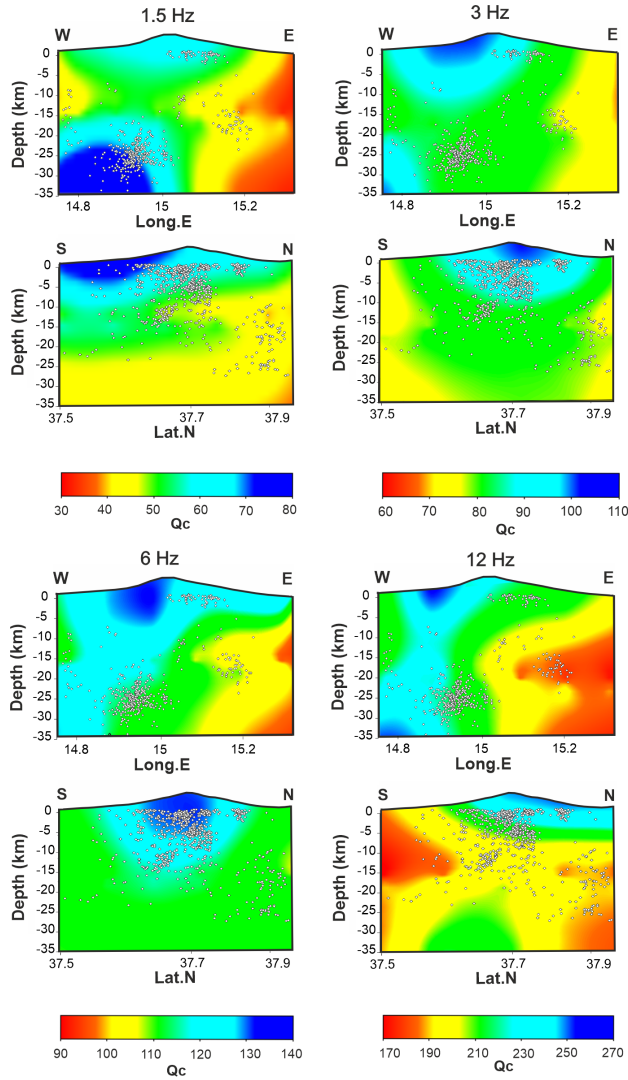


Figure 6: North-South and East-West Vertical sections correspondent to the black dotted lines reported in Figure 1, for the frequency bands centered at 1.5, 3.0, 6 and 12Hz. Superimposed are the main topographical features and the earthquake sources. The color scale represents  $Q_c$ .

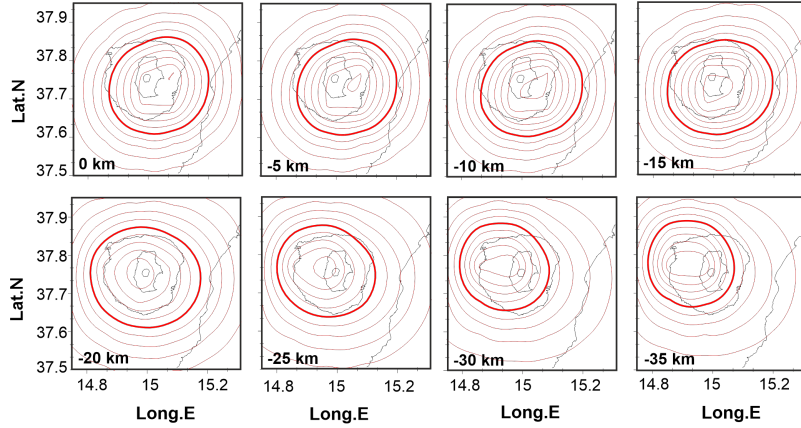


Figure 7: Slices of the Resolution cut from 0 to 35 km. Isolines (in red) start from the value of 0.1 to 0.9. The thickest isolines represent the value of 0.5.

367 The Resolution,  $R_j$ , is determined according to the equation (10) of Ap-  
 368 pendix 2, while the uncertainties associated with  $Q_{cj}$  values are estimated  
 369 using equation (9) in Appendix 2. The isolines of equal  $R_j$  are shown in  
 370 Figure 7.

371 Uncertainties on  $Q_{cj}$  fall in the interval between 3 and 10. We thus  
 372 decided to draw isolines spaced of 10 units in the images of Figures 4, 5,  
 373 6. The volume under study, which spans the whole Etna area, roughly  
 374 corresponds to the zones with Resolution greater than 0.1; this value is  
 375 associated with uncertainties of the order of 10 on  $Q_{cj}$ .

## 376 4 Discussion

377 Differently from non-volcanic areas (see e.g. Akinci et al., 2020),  $Q_c$  av-  
 378 eraged over the events in the Mt. Etna area indicate high attenuation for  
 379 any frequency band, as expected for an highly heterogeneous and complex

380 volcanic region (Table 1). Moreover, the same Table shows that  $Q_c$  in the  
381 shallowest part of the crust and in the lower crust/upper mantle are practi-  
382 cally coincident, indicating that attenuation does not decrease with depth in  
383 the first 35 km beneath Etna. While several studies (see e.g. Ibañez et al.,  
384 1990) show that in general  $Q$  grows with depth, in our analysis, differently,  
385 we observe an almost uniform pattern, and in some areas even a decrease  
386 of  $Q$ -coda (increase of the attenuation) with depth. Consequently, at Mt  
387 Etna volcano the effect of the upper crust and lateral heterogeneity should  
388 be stronger than any depth dependence, contrarily to what is observed in  
389 other regions.

390 The average  $Q_c$  values (Table 1) and the images of Figure 4 and 5, and  
391 6, show that a)  $Q_c$  changes with the frequency bands investigated and b)  
392 the space attenuation anomalies change their intensity with increasing fre-  
393 quency. The interpretation of the dependence of  $Q_c$  on frequency is open  
394 to discussion, as the physical meaning of  $Q_c$  itself is controversial, as com-  
395 mented in Section 3.1. First,  $Q_c$  has an unclear physical meaning; second, it  
396 is an estimate of a combination of intrinsic- and scattering- $Q$  which depends  
397 on the scattering regime in the zone of analysis; third, the model used to fit  
398 the observed Energy Envelopes assumes point-like scatterers, and uniform  
399 scattering. The frequency dependence may reasonably depend on the ratio  
400 between the wavelength and the average scatterer size, indicating how much  
401 the experimental reality differs from the model assumptions. In this paper  
402 we assume that the waves with high wavelength ( $< 6$  Hz) could be affected  
403 by discontinuities and heterogeneities at large scale, while the coda waves in  
404 the 12 Hz band better reflect the smaller scale structures.

405 In the following we first briefly identify and discuss the presence of areas  
406 characterized by in depth and/or lateral attenuation contrasts. After that,  
407 we make an interpretation in the framework of the seismological, geological  
408 and volcanological evidences together with the other velocity and attenuation  
409 images already available in the area. The first evidence is that the observed  
410 anomalies of  $Q_c$  can be associated with areas dominated by high structural  
411 complexities and are distributed along well-known tectonic structures which  
412 characterize the upper crust in the region of Etna volcano.

413 As discussed above (Subsection 3.5), we assume that  $Q_c$  at low frequency  
414 (1.5 Hz) is close to  $Q_s$ . Consequently, the attenuation is almost entirely  
415 produced by strongly heterogeneous structures, like faults or fractures, which  
416 pump back the seismic energy to the receiver by reflection or refraction. The  
417 comparison with the 2D image of separate  $Q_i$  and  $Q_s$  shown in Ibáñez et al.  
418 (2020) may be difficult, as the 2D separate  $Q_i$  and  $Q_s$  images represent  
419 the attenuation in a shallow and thin (2km thick) layer where most of the  
420 attenuation phenomena are governed by scattering. The present image at  
421 the shallowest depth, on the contrary, represent the first 5 km of crust below  
422 the surface, marked by a smaller average heterogeneity.

423 In detail, the  $Q_c$  contrasts observed at 1.5 Hz (Figures 4 and 6) are  
424 consistent with the direction of the most visible structural system present  
425 in the eastern flank of Mt. Etna volcano (Figure 1). Here, seismogenic  
426 faults NNW-SSE oriented along which the shallow seismicity ( $h \leq 10$  km)  
427 is concentrated (Timpe Faults System, TFS; Figure 1), represent the north-  
428 ernmost elongation of the Malta Escarpment, the main lithospheric structure  
429 in eastern Sicily (Bousquet and Lanzafame, 2004). The  $Q_c$  contrasts delimit

430 a wide volume marked by medium to high  $Q_c$ , elongated in the NW-SE direc-  
431 tion, mostly extending from the southern flank of the volcanic edifice towards  
432 southeast. It is worth stressing that this high  $Q_c$  anomaly spatially correlates  
433 with the location of a high velocity body, named in several works as HVB,  
434 and placed by many authors in the central-southern sector of Mt. Etna and  
435 extending toward the eastern area, as evidenced in literature (e.g. Patanè  
436 et al., 2002; Barberi et al., 2004; De Gori et al., 2005; Martinez-Arevalo  
437 et al., 2005; Patanè et al., 2006; De Gori et al., 2011; Alparone et al., 2012).  
438 This huge HVB has been recently well resolved by a recent velocity tomog-  
439 raphy ( $V_p$  and the ratio  $V_p/V_s$ ) study, showing a refined structure from the  
440 surface up to a depth of 18 km (Giampiccolo et al., 2020), representing a  
441 massive accumulation of non-erupted volcanic material, emplaced during the  
442 recent and past volcanic activity in the sedimentary basement (Corsaro et al.,  
443 2004). Is very interesting to observe another high-velocity/high-Q anomaly  
444 placed in the South-East region of Mt. Etna, previously highlighted by Díaz-  
445 Moreno et al. (2018) and by Ibáñez et al. (2020) too. This last region can  
446 be correlated with a magnetic positive anomaly, considered as large and in-  
447 tense ( $>700$  nT), that Cavallaro et al. (2016) associated with deep magmatic  
448 sources. Corsaro et al. (2004) explained that these magmatic bodies could  
449 be compatible with the existence of a feeding system of an ancient shield  
450 volcano located offshore of the Timpe area. At 3 and 6 Hz  $Q_c$  tends to be  
451 similar to  $Q_t$ , as observed by Del Pezzo et al. (2019). In general, higher  
452  $Q_c$  values predominate in the western part of the volcano more than in the  
453 eastern flank. This finding is consistent with the structural setting of the  
454 western part of Mt. Etna which is considered as the most stable. A ma-

455 jor high  $Q_c$  zone, oriented NE-SW is clearly visible down to the depth of  
456 5 km and vanishes at greater depths. Its southern edge is oriented along  
457 the direction of the Rift W (Figure 1) which constitutes a structural limit  
458 between a very unstable flank, placed on the Southwest, and the observed  
459 steady zone toward the Northwest. A minor high  $Q_c$  anomaly, visible only at  
460 6 Hz in the same depth range, is observed ENE of the volcanic edifice. The  
461 location of this low attenuation volume, E-W oriented, is coincident with  
462 the position of the eastern segment of the PF (Figure 1). This structure  
463 has an important role in controlling the dynamic of the eastern sector and  
464 represents the intersection between an unstable and a stable area (Alparone  
465 et al., 2013). At high frequency (12 Hz) intrinsic dissipation predominates  
466 over the scattering; consequently, the attenuation measured by  $Q_c$  is mainly  
467 attributable to an absorption effect. The images at high (12 Hz) frequency  
468 (Figure 5 and 6) show the strongest attenuation contrasts at all depths, with  
469  $Q_c$  changes up to 30% with respect to the average. The first feature is a high  
470  $Q_c$  anomaly located in the western sector of the volcano, approximately in  
471 the same position of the anomaly observed at 3 and 6 Hz. A second high  $Q_c$   
472 anomaly is located to the NE of the summit craters. This anomaly correlates  
473 with a high P-wave velocity volume observed by Giampiccolo et al. (2020),  
474 close to the central-western sector of PF (Figure 1). The western limit of this  
475 anomaly marks the boundary with a highly fractured zone corresponding to  
476 the NE Rift (Figure 1), one of the zones where is placed a main magma  
477 intrusion below the volcano. On the eastern side, a low  $Q_c$  lobe extends  
478 from the crater area toward southeast, and coincides with the zone where  
479 most of the shallow fractures are located. In overall, at all frequencies, low

480  $Q_c$  mostly characterize the whole investigated area up to the depth of 20  
481 km. It is worth stressing that low  $V_p$  and high  $V_p/V_s$  have been observed all  
482 around the volcanic edifice, up to 18 km b.s.l. by Giampiccolo et al. (2020).  
483 As also reported by these authors, the association of low  $V_p$  with low  $Q_p$  and  
484 high  $V_p/V_s$  testifies the possible presence around Mt. Etna of large volumes  
485 of over-pressurized fluids within the sedimentary units. In many of these  
486 zones it is observed a large rate of seismicity that can be the consequence  
487 of micro-cracking generated by the high pore-pressure (Giampiccolo et al.,  
488 2020). Some high  $Q_c$  volumes are observed to the west of the volcanic ed-  
489 ifice. At 1.5 and 12 Hz these volumes correlate well with the distribution  
490 of the deep seismicity (20-35 km), which characterizes the western sector  
491 of the volcano. This sector, according to literature, is linked with the re-  
492 gional tectonic processes associated with the compressive regime at the front  
493 of the Apennine Maghrebian Chain (Catalano et al. 2004; Lavecchia et al.  
494 2007; Sicali et al. 2014; De Guidi et al. 2014; Scarfi et al. 2016). The deep  
495 seismicity has been indicated by Lavecchia et al., 2007 as originated from  
496 segments of the so called “Sicilian Basal Thrust”, a regional scale deep crustal  
497 structure. The existence of this geological structure was confirmed on the  
498 base of earthquake focal mechanisms, geodetic data and field studies, which  
499 indicated the evidence of active folds and thrust deformation zones located  
500 South of the volcanic edifice (De Guidi et al., 2014).

## 501 5 Conclusions

502 3D direct P-wave or S-wave attenuation (total-Q,  $Q_t$ ) tomography is con-  
503 firmed as one of the most useful tools to image geological structures in  
504 general; in particular, for volcano structures, this procedure is very inter-  
505 esting since permits to associate physical parameters related to the decrease  
506 of transmitted energy with the feeding conduits and magma chambers, con-  
507 tributing to the modeling of volcano dynamics. However, despite this posi-  
508 tive prospective, some difficulty arises in the geological interpretation, mainly  
509 due to the difficulty in associating the seismic attenuation attributes with  
510 rock properties (Nolet, 2008). In volcanic areas attenuation tomography  
511 techniques based on the analysis of direct waves are mainly based on the  
512 measurement of the sole P-wave attenuation. Conversely, the information  
513 derived from the S-wave attenuation results to be is extremely useful in the  
514 interpretation of the volcanic dynamic and rock properties, as they are di-  
515 rectly associated for example with the thermally weakened crust in volcanoes,  
516 much more than P-wave attenuation anomalies, among other characteristics.

517 As we have evidenced in the present work, the diffusive (scattering) wave  
518 field can entirely fill this lack, since coda waves are predominantly composed  
519 by S-waves, and they are much more easily analyzable than the direct S-  
520 waves. This is the reason why the study of the space distribution of  $Q_c$  values  
521 is now starting to be used to improve the reconstructions of the tectonic  
522 and geological features at a crustal-scale, providing additional information  
523 about the fluid content. In this study, for the first time we employ a 3D  
524 approach based on the Q-coda attenuation kernels to map shallow crust and

525 upper mantle in the Mt. Etna area at different frequencies. This approach  
526 provides a marked improvement in the geological interpretation, if compared  
527 with the information given by the measure of  $Q_c$  averaged over the area. The  
528 present study adds details in the medium characteristics at the roots of Mt.  
529 Etna, and helps to understand the tectonic complexity of the crust and  
530 upper mantle of this region by observing the pattern of the attenuation of  
531 seismic waves. This is mainly because it is based on the analysis of (single or  
532 multiple) scattered waves sampling large volumes of the volcanic structure,  
533 and covering wider regions than the analysis of direct waves. In the upper  
534 crust regions of highest structural complexities are associated with evident  
535  $Q_c$  anomalies and they are distributed along well known tectonic structures  
536 in the crust beneath Mt. Etna. In every frequency band, low  $Q_c$  values (as  
537 compared with a world average) mostly characterize the whole investigated  
538 area, in agreement with low  $V_p$  and high  $V_p/V_s$  observed all around the  
539 volcanic edifice, down to 18 km b.s.l. by Giampiccolo et al. (2020). Following  
540 these authors our results confirm the existence of a very large hydrothermal  
541 system, placed in depth, associated with the sedimentary units placed around  
542 the volcanic edifice that contain wide volumes over-pressured by fluids. In  
543 the middle crust/upper mantle transition zone, below 20 km of depth, the  
544 present images show a structure more homogeneous than that at shallower  
545 depth. High  $Q_c$  volumes, observed to the west of the volcanic edifice, are  
546 correlated with the regional tectonic dynamics. The present results add  
547 information about the lower crust/upper mantle, between the depths of 20  
548 and 35 km, where previous information was only marginal. However, as  $Q_c$   
549 is a complex combination of the inelastic and scattering attenuation, the

550 interpretation is still incomplete. A separate ( $Q_i$  and  $Q_s$ ) three dimensional  
551 attenuation image is still quite hard to obtain, due to the intrinsic difficulties  
552 in estimating separate observables in a single seismogram. This achievement  
553 will be our challenge for future studies.

## 554 **6 Acknowledgements**

555 Anonymous Reviewers and Associate Editor's comments greatly improved  
556 the quality of the manuscript. This work was partially funded by the Span-  
557 ish Mineco Project FEMALE, PID2019-106260GB-I00 and Paneta Dinamico  
558 (INGV 2021). Author contributions: E. Del Pezzo, E. Giampiccolo and T.  
559 Tuvè analyzed the results and prepared the Figures; T. Tuvé and E. Gi-  
560 ampiccolo prepared the data base; G. Di Grazia supervised the Geological  
561 part; J.M. Ibañez, E. Del Pezzo and E. Giampiccolo supervised the text  
562 draft.

## 563 **References**

- 564 Aki, K. and B. Chouet (1975). Origin of coda waves: Source, atten-  
565 uation, and scattering effects. *Journal Of Geophysical Research-Solid*  
566 *Earth* 80(23), 3322–3342.
- 567 Akinci, A., E. Del Pezzo, and L. Malagnini (2020). Intrinsic and scattering  
568 seismic wave attenuation in the Central Apennines (Italy). *Physics of the*  
569 *Earth and Planetary Interiors* 303, 106498.
- 570 Aloisi, M., O. Cocina, G. Neri, B. Orecchio, and E. Privitera (2002). Seismic

571 tomography of the crust underneath the Etna volcano, Sicily. *Phys. Earth*  
572 *Planet. Inter.* 134, 139–155.

573 Alparone, S., G. Barberi, O. Cocina, E. Giampiccolo, C. Musumeci, and  
574 D. Patanè (2012). Intrusive mechanism of the 2008–2009 Mt. Etna erup-  
575 tion: Constraints by tomographic images and stress tensor analysis. *Jour-*  
576 *nal Of Volcanology And Geothermal Research* 229-230, 50–63.

577 Alparone, S., O. Cocina, S. Gambino, A. Mostaccio, S. Spampinato, T. Tuvè,  
578 and A. Ursino (2013). Seismological features of the Pernicana-Provenzana  
579 Fault System (Mt. Etna, Italy) and implications for the dynamics of north-  
580 eastern flank of the volcano. *Journal of Volcanology and Geothermal Re-*  
581 *search* 118, 1 – 11.

582 Alparone, S., V. Maiolino, A. Mostaccio, A. Scaltrito, A. Ursino, G. Bar-  
583 beri, G. Di Grazia, E. Giampiccolo, C. Musumeci, L. Scarfi, and L. Zuc-  
584 carello (2015). Instrumental seismic catalogue of Mt. Etna earthquakes  
585 (Sicily, Italy): ten years (2000-2010) of instrumental recordings. *Ann.*  
586 *Geophys* 58(4), S0435.

587 Alparone, S. C., G. Barberi, S. D’Amico, G. Di Grazia, F. Ferrari,  
588 E. Giampiccolo, V. Maiolino, A. Mostaccio, C. Musumeci, A. Scaltrito,  
589 L. Scarfi, M. Sciotto, S. Spampinato, G. Tusa, T. Tuvè, A. Ursino, and  
590 L. Zuccarello (2020). *Mt. Etna Revised and Concise Seismic Catalog from*  
591 *1999 (EtnaRCSC) [Data set].*, Volume Istituto Nazionale di Geofisica e  
592 Vulcanologia (INGV),.

593 Azzaro, R., G. Barberi, S. D’Amico, B. Pace, L. Peruzza, and T. Tuvè

594 (2017). When probabilistic seismic hazard climbs volcanoes: the Mt.  
595 Etna case, Italy – Part 1: Model components for sources parameterization.  
596 *Nat. Hazards Earth Syst. Sci.* 17([https://doi.org/10.5194/nhess-17-1981-](https://doi.org/10.5194/nhess-17-1981-2017)  
597 2017.), 1981–1998.

598 Azzaro, R., S. Branca, K. Gwinner, and M. Coltelli (2012). The volcano-  
599 tectonic map of Etna volcano, 1:100.000 scale: an integrated approach  
600 based on a morphotectonic analysis from high-resolution DEM con-  
601 strained by geologic, active faulting and seismotectonic data. *Ital. J.*  
602 *Geosci.* 131(1), 153–170.

603 Azzaro, R., S. D’Amico, L. Peruzza, and T. Tuvè (2013). Probabilistic  
604 seismic hazard at Mt. Etna (Italy): the contribution of local fault activity  
605 in mid-term assessment. *J. Volcanol. Geotherm. Res. In special issue: flank*  
606 *instability at Mt. Etna, Acocella V, Puglisi P, Amelung F (Eds).*(251),  
607 158–169.

608 Barberi, G., M. Cosentino, A. Gervasi, I. Guerra, G. Neri, and B. Orecchio  
609 (2004). Crustal seismic tomography in the Calabrian Arc region, South  
610 Italy. *Phys. Earth Planet. Interiors* 147(297-314).

611 Bonforte, A. and G. Puglisi (2003). Magma uprising and flank dynamics on  
612 Mount Etna volcano, studied using GPS data (1994–1995). *J. Geophys.*  
613 *Res. Solid Earth* 108(2153).

614 Borgia, A., L. Ferrari, and G. Pasquarè (1992). Importance of gravitational  
615 spreading in the tectonic and volcanic evolution of Mount Etna. *Na-*  
616 *ture* 357, 231–235.

- 617 Bousquet, J. and G. Lanzafame (2004). *The tectonics and geodynamics of*  
618 *Mt. Etna: synthesis and interpretation of geological and geophysical data,*  
619 Volume In: Bonaccorso, A., Calvari, S., Coltelli, M., Del Negro, C., Fal-  
620 saperla, S. (Eds.) Etna Volcano Laboratory. AGU (Geophysical mono-  
621 graph series).
- 622 Branca, S. and V. Ferrara (2013). The morphostructural setting of Mount  
623 Etna sedimentary basement (Italy): Implications for the geometry and  
624 volume of the volcano and its flank instability. *Tectonophysics* 586, 46 –  
625 64.
- 626 Calvet, M., M. Sylvander, L. Margerin, and A. Villasenor (2013). Spatial  
627 variations of seismic attenuation and heterogeneity in the Pyrenees: Coda  
628 Q and peak delay time analysis. *Tectonophysics* 608, 428–439.
- 629 Cardaci, C., M. Coviello, G. Lombardo, G. Patanè, and R. Scarpa (1993).  
630 Seismic tomography of Etna volcano. *J. VolcanoL Geotherm. Res.* 56,  
631 357–368.
- 632 Cassinis, R., I. Finetti, P. Giese, C. Morelli, L. Steinmetz, and O. Vec-  
633 chia (1969). Deep seismic refraction research on Sicily. *Boll. Geof. Teor.*  
634 *Appl.* 11, 140–160.
- 635 Catalano, S., S. Torrisi, and C. Ferlito (2004). The relationship between Late  
636 Quaternary deformation and volcanism of Mt. Etna (eastern Sicily): new  
637 evidence from the sedimentary substratum in the Catania region. *Journal*  
638 *of Volcanology and Geothermal Research* 132, 311–344.

- 639 Cavallaro, D., L. Cocchi, M. Coltelli, F. Muccini, C. Carmisciano,  
640 M. Firetto Carlino, J. Ibáñez, D. Patanè, M. Filippone, and E. Buttaro  
641 (2016). Acquisition procedures, processing methodologies and preliminary  
642 results of magnetic and ROV data collected during the TOMO-ETNA  
643 experiment. *Annals of Geophysics* 59(4), S0431.
- 644 Chiarabba, C., A. Amato, E. Boschi, and F. Barberi (2000). Recent seis-  
645 micity and tomographic modeling of the Mount Etna plumbing system. *J.*  
646 *Geophys. Res.* 105, 10923–10938.
- 647 Chiarabba, C., P. De Gori, and D. Patanè (2004). *The Mt. Etna plumb-*  
648 *ing system: the contribution of seismic tomography*, Volume Etna volcano  
649 laboratory. Geophysical Monograph Series, AGU.
- 650 Clocchiatti, R., M. Condomines, N. Guenot, and J. Tanguy (2004). Magma  
651 changes at Mount Etna: the 2001 and 2002–2003 eruptions. *Earth and*  
652 *Planetary Science Letters* 226, 397 – 414.
- 653 Continisio, R., F. Ferrucci, G. Gaudiosi, D. Lo Bascio, and G. Ventura  
654 (1997). Malta escarpment and Mt. Etna: early stages of an asymmet-  
655 ric rifting process? Evidences from geophysical and geological data. *Acta*  
656 *Vulcanol.* 9, 45–53.
- 657 Corsaro, R. A., S. G. Rotolo, O. Cocina, and G. Tumbarello (2004). Cognate  
658 xenoliths in Mt. Etna lavas: witnesses of the high-velocity body beneath  
659 the volcano. *Bull Volcanol* 76(816), 12 pp.
- 660 De Gori, P., C. Chiarabba, E. Giampiccolo, C. Martinez-Arevalo, and

- 661 D. Patanè (2011). Body wave attenuation heralds incoming eruptions  
662 at Mount Etna. *Geology* 39(5), 503 – 506.
- 663 De Gori, P., C. Chiarabba, E. Giampiccolo, C. Martinez-Arevalo, and  
664 D. Patanè (2011). Body wave attenuation heralds incoming eruptions  
665 at Mt. Etna. *Geology* 39, 503–506.
- 666 De Gori, P., C. Chiarabba, and D. Patanè (2005). Qp structure of Mount  
667 Etna: constraints for the physics of the plumbing system. *J. Geophys.*  
668 *Res.* 110(B05303)(doi:10.1029/2003JB002875.).
- 669 De Guidi, G., S. Imposa, S. Scudero, and M. Palano (2014). New evidence  
670 for Late Quaternary deformation of the substratum of Mt. Etna volcano  
671 (Sicily, Italy): clues indicate active crustal doming. *Bull. Volcanol.*
- 672 De Siena, L., M. Calvet, K. J. Watson, A. R. T. Jonkers, and C. Thomas  
673 (2016). Seismic scattering and absorption mapping of debris flows, feed-  
674 ing paths, and tectonic units at Mount St. Helens volcano. *Earth And*  
675 *Planetary Science Letters* 442(C), 21–31.
- 676 De Siena, L., E. Del Pezzo, C. Thomas, A. Curtis, and L. Margerin (2013,  
677 October). Seismic energy envelopes in volcanic media: in need of boundary  
678 conditions. *Geophysical Journal International* 195(2), 1102–1119.
- 679 Del Pezzo, E. (2008). Seismic Wave Scattering in Volcanoes. *Advances in*  
680 *Geophysics, Vol 50* 50, 353–371.
- 681 Del Pezzo, E., F. Bianco, E. Giampiccolo, G. Tusa, and T. Tuve (2015). A

682 reappraisal of seismic Q evaluated at Mt. Etna volcano. Receipt for the  
683 application to risk analysis. *Journal Of Seismology* 19, 105 – 119.

684 Del Pezzo, E., A. De La Torre, F. Bianco, J. M. Ibañez, S. Gabrielli, and  
685 L. De Siena (2018). Numerically Calculated 3D Space-Weighting Func-  
686 tions to Image Crustal Volcanic Structures Using Diffuse Coda Waves.  
687 *Geosciences* 8(5), 175–13.

688 Del Pezzo, E., E. Giampiccolo, T. Tuvè, G. Di Grazia, S. Gresta, and  
689 J. Ibañez (2019). Study of the regional pattern of intrinsic and scatter-  
690 ing seismic attenuation in Eastern Sicily (Italy) from local earthquakes.  
691 *Geophys. J. Int.* 218(doi: 10.1093/gji/ggz208), 1456–1468.

692 Del Pezzo, E. and J. M. Ibañez (2020). Seismic coda-waves imaging based on  
693 sensitivity kernels calculated using an heuristic approach. *Geosciences* 10,  
694 304.

695 Del Pezzo, E., J. Ibañez, J. Prudencio, F. Bianco, and L. De Siena (2016).  
696 Absorption and scattering 2-D volcano images from numerically calculated  
697 space-weighting functions. *Geophys. J. Int* 206, 742–756.

698 Díaz-Moreno, A., G. Barberi, O. Cocina, I. Koulakov, L. Scarfi, L. Zuc-  
699 carello, J. Prudencio, A. Garcia-Yeguas, I. Alvarez, L. Garcia, and J. M.  
700 Ibañez (2018). New insights on Mt. Etna’s Crust and relationship with the  
701 regional tectonic framework from joint active and passive P-wave seismic  
702 tomography. *Surv. Geophys.* 39(1), 57 – 97.

703 Eulenfeld, T. and U. Wegler (2016). 2016. measurement of intrinsic and

704 scattering attenuation of shear waves in two sedimentary basins and com-  
705 parison to crystalline sites in germany,. *Geophys. J. Int.*, 205, 744–757.

706 Eulenfeld, T. and U. Wegler (2017). Crustal intrinsic and scattering attenua-  
707 tion of high-frequency shear waves in the contiguous united states. *Journal*  
708 *of Geophysical Research: Solid Earth* 122(6), 4676–4690.

709 Faccenna, C., T. Becker, F. Lucente, L. Jolivet, and F. Rossetti  
710 (2001). History of subduction and back-arc extension in the central  
711 Mediterranean. *Geophys. J. Int.* 145([http://dx.doi.org/10.1046/j.0956-](http://dx.doi.org/10.1046/j.0956-540x.2001.01435.x)  
712 540x.2001.01435.x), 809 – 820.

713 Federico, C., M. Longo, W. D’Alessandro, S. Bellomo, P. Bonfanti, and  
714 L. Brusca (2017). Hydrological versus volcanic processes affecting fluid  
715 circulation at Mt. Etna: Inferences from 10 years of observations at the  
716 volcanic aquifer. *Chemical Geology.* 452.

717 Gaebler, P. J., T. Eulenfeld, and U. Wegler (2015). Seismic scattering  
718 and absorption parameters in the w-bohemia/vogtland region from elas-  
719 tic and acoustic radiative transfer theory. *Geophysical Journal Interna-*  
720 *tional* 203(3), 1471–1481.

721 Giampiccolo, E., O. Cocina, P. De Gori, and C. Chiarabba (2020). Dyke  
722 intrusion and stress-induced collapse of volcano flanks: The example of  
723 the 2018 event at Mt. Etna (Sicily, Italy). *Nature Research - Scientific*  
724 *Reports* (10:6373 <https://doi.org/10.1038/s41598-020-63371-3>).

725 Giampiccolo, E. and T. Tuvè (2018). Regionalization and dependence of

726 coda Q on frequency and lapse time in the seismically active Peloritani  
727 region (Northeastern Sicily, Italy). *J. Seismol.* *22*(4), 1059–1074.

728 Gvirtzman, Z. and A. Nur (1999). The formation of Mount Etna as the  
729 consequence of slab rollback. *Nature* *401*, 782–785.

730 Hirn, A., A. Nercessian, M. Sapin, F. Ferrucci, and G. Wittlinger (1991).  
731 Seismic heterogeneity of Mt. Etna: structure and activity. *Geophys.*  
732 *J.Int.* *105*, 139–153.

733 Hirn, A., R. Nicolich, and J. Gallart (1997). Roots of Etna volcano in faults  
734 of great earthquakes. *Earth Planet. Sci. Lett.*, *148*, 171–191.

735 Ibañez, J. M., E. Del Pezzo, M. Herraiz, G. Alguacil, and J. Morales  
736 (1990). Depth-dependent seismic attenuation in the Granada zone (South-  
737 ern Spain). *Bulletin of The Seismological Society of America* *80*(5), 1232–  
738 1244.

739 Ibáñez, J. M., I. Castro-Melgar, O. Cocina, L. Zuccarello, S. Branca,  
740 E. Del Pezzo, and J. Prudencio (2020). First 2-d intrinsic and scatter-  
741 ing attenuation images of Mt Etna volcano and surrounding region from  
742 active seismic data. *Geophysical Journal International* *220*(1), 267–277.

743 Laigle, M., A. Hirn, M. Sapin, J.-C. L epine, J. Diaz, and J. Gallart (2000).  
744 Mount Etna dense array local earthquake P and S tomography and impli-  
745 cations for volcanic plumbing. *J. Geophys. Res.* *105*,, 21633–21646.

746 Larose, E., T. Planes, V. Rossetto, and L. Margerin (2010). Locating a

747 small change in a multiple scattering environment. *Applied Physics Let-*  
748 *ters* 96(20), 204101.

749 Lavecchia, G., F. Ferrarini, R. De Nardis, F. Visini, and M. S. Barbano  
750 (2007). Active thrusting as a possible seismogenic source in Sicily (South-  
751 ern Italy): Some insights from integrated structural kinematic and seis-  
752 mological data. *Tectonophysics* 445(145–167).

753 Lentini, F. (1982). The geology of the Etna basement. *Mem. Soc. Geol.*  
754 *Ital.* 23, 7–25,.

755 Lo Giudice, E., , and Rasà (1992). Very shallow earthquakes and brit-  
756 tle deformation in active volcanic areas: The Etnean region as example.  
757 *Tectonophysics* 202, 257–268.

758 Margerin, L. (2011, December). Seismic waves, scattering. *Encyclopedia of*  
759 *solid earth geophysics*, 1210–1223.

760 Margerin, L., T. Planes, J. Mayor, and M. Calvet (2016). Sensitivity ker-  
761 nels for coda-wave interferometry and scattering tomography: theory and  
762 numerical evaluation in two-dimensional anisotropically scattering media.  
763 *Geophys. J. Int.* 204, 650–666.

764 Martinez-Arevalo, C., D. Patanè, A. Rietbrock, and Ibañez, J.M. (2005). The  
765 intrusive process leading to the Mt. Etna 2001 flank eruption: Constraints  
766 from 3-D attenuation tomography. *Geophysical Research Letters* 32(21),  
767 L21309.

768 Mayeda, K., S. Koyanagi, M. Hoshiaba, K. Aki, and Y. Zeng (1992). A

769 comparative study of scattering, intrinsic, and coda Q-1 for Hawaii, Long  
770 Valley, and central California between 1.5 and 15 Hz. *J. Geophys. Res* 97,  
771 6643–6659.

772 Mayor, J., M. Calvet, L. Margerin, O. Vanderhaeghe, and P. Traversa (2016).  
773 Crustal structure of the Alps as seen by attenuation tomography. *Earth*  
774 *and Planetary Science Letters* 439, 71 – 80.

775 Mayor, J., L. Margerin, and M. Calvet (2014). Sensitivity of coda waves to  
776 spatial variations of absorption and scattering: radiative transfer theory  
777 and 2-D examples. *Geophysical Journal International* 197(2), 1117–1137.

778 Mostaccio, A., T. Tuvè, D. Patanè, G. Barberi, and L. Zuccarello (2013).  
779 Improving seismic surveillance at Mt. Etna volcano by probabilistic earth-  
780 quake location in a 3D model. *B. Seismol. Soc. Am.* 103(4), 2447–2459.

781 Musumeci, C., O. Cocina, P. De Gori, and D. Patanè (2004). Seismological  
782 evidence of stress induced by dike injection during the 2001 Mt. Etna  
783 eruption. *Geophys. Res. Lett.* 31 L07617.(doi: 10.1029/2003GL019367.).

784 Nolet, G. (2008). *A Breviary of Seismic Tomography: Imaging the Interior*  
785 *of the Earth and Sun*. Cambridge: Cambridge University Press.

786 Obermann, A., T. Planès, E. Larose, C. Sens-Schönfelder, and M. Campillo  
787 (2013). Depth sensitivity of seismic coda waves to velocity perturba-  
788 tions in an elastic heterogeneous medium. *Geophysical Journal Interna-*  
789 *tional* 194(1), 372–382.

- 790 Ogniben, L. (1966). Lineamenti idrogeologici dell' Etna. *Riv. Miner.*  
791 *Sicil. 100–102*, 24 pp.
- 792 Paasschens, J. (1997). Solution of the time-dependent Boltzmann equation.  
793 *Physical Review E 56*(1), 1135 – 1141.
- 794 Pacheco, C. and R. Snieder (2006). Time-lapse travelttime change of  
795 singly scattered acoustic waves. *Geophysical Journal International* doi:  
796 [10.1111/j.1365-246X.2006.02856.x](https://doi.org/10.1111/j.1365-246X.2006.02856.x)(165), 485 – 500.
- 797 Patanè, D., M. Aliotta, A. Cannata, C. Cassisi, M. Coltelli, G. Di Grazia,  
798 P. Montalto, and L. Zuccarello (2011). Interplay between Tectonics and  
799 Mount Etna's Volcanism: Insights into the Geometry of the Plumbing  
800 System. *IntechOpen*.
- 801 Patanè, D., G. Barberi, O. Cocina, P. De Gori, and C. Chiarabba (2006).  
802 Time-resolved seismic tomography detects magma intrusions at Mount  
803 Etna. *Science 313*, 821–823.
- 804 Patanè, D., C. Chiarabba, O. Cocina, P. De Gori, M. Moretti, and E. Boschi  
805 (2002). Tomographic images and 3D earthquake locations of the seismic  
806 swarm preceding the 2001 Mt. Etna eruption: Evidence for a dyke intru-  
807 sion. *Geophys. Res. Lett.*, *29*(10), 135 1 – 134 4.
- 808 Patanè, D., O. Cocina, S. Falsaperla, E. Privitera, and S. Spampinato (2004).  
809 Mt. etna volcano: a seismological framework. *in: Mt. Etna: Volcano Labo-*  
810 *ratory, edited by: Calvari, S., Bonaccorso, A., Coltelli, M., Del Negro, C.,*  
811 *and Falsaperla, S., Am. Geophys. Union, Geophys. Monogr., 143, Wash-*  
812 *ington, D.C., 147–165..*

- 813 Planès, T., E. Larose, L. Margerin, V. Rossetto, and C. Sens-Schönfelder  
814 (2014). Decorrelation and phase-shift of coda waves induced by local  
815 changes: multiple scattering approach and numerical validation. *Waves in*  
816 *Random and Complex Media* 24(2), 99–125.
- 817 Prudencio, J., L. De Siena, J. M. Ibanez, E. Del Pezzo, A. Garcia Yeguas,  
818 and A. Díaz-Moreno (2015). The 3D Attenuation Structure of Deception  
819 Island (Antarctica). *Surveys in Geophysics* 36(3), 371 – 390.
- 820 Prudencio, J., E. Del Pezzo, A. Garcia Yeguas, and J. M. Ibanez (2013-a).  
821 Spatial distribution of intrinsic and scattering seismic attenuation in active  
822 volcanic islands - I: model and the case of Tenerife Island. *Geophysical*  
823 *Journal International* 195(3), 1942–1956.
- 824 Prudencio, J., J. M. Ibanez, A. Garcia Yeguas, E. Del Pezzo, and A. M.  
825 Posadas (2013-b). Spatial distribution of intrinsic and scattering seismic  
826 attenuation in active volcanic islands - II: Deception Island images. *Geo-*  
827 *physical Journal International* 195(3), 1957 – 1969.
- 828 Prudencio, J., T. Taira, Y. Aoki, H. Aoyama, and S. Onizawa (2017). In-  
829 trinsic and scattering attenuation images of usu volcano, japan. *Bulletin*  
830 *of Volcanology* 79(4), 29.
- 831 Rittmann, A. (1973). Structure and evolution of Mount Etna. *Phil. Trans.*  
832 *Roy. Soc., London*, 274 A, 5–16.
- 833 Rust, D., B. Behncke, M. Neri, and A. Ciocanel (2005). Nested zones of in-  
834 stability in the Mount Etna volcanic edifice, Sicily. *J. Volcanol. Geotherm.*  
835 *Res.* 144, 137–153.

- 836 Rust, D. and M. Neri (1996). The boundaries of large-scale collapse on the  
837 flanks of Mount Etna, Sicily. *In: Volcano instability on the Earth and*  
838 *other planets. McGuire, W.J., Jones, A.P., Neuberg, J., Geol. Soc. Lond.*  
839 *Spec. Pub. (110.), 193–208.*
- 840 Sato, H. (1977). Energy propagation including scattering effects. single  
841 isotropic scattering approximation. *Journal of Physics of the Earth 25(1),*  
842 *27–41.*
- 843 Sato, H., M. Fehler, and T. Maeda (2012). *Seismic wave propagation and*  
844 *scattering in the heterogeneous Earth Second Edition.* Springer-Verlag.
- 845 Scarfì, L., G. Barberi, C. Musumeci, and D. Patanè (2016). Seismotecton-  
846 ics of northeastern Sicily and southern Calabria (Italy): new constraints  
847 on the tectonic structures featuring in a crucial sector for the Central  
848 Mediterranean geodynamics. *Tectonics 34,* 812–832.
- 849 Sharp, A., P. Davis, F. Gray, and G. King (1980). Preliminary results from a  
850 seismic array study of Mount Etna, United Kingdom Research on Mount  
851 Etna 1977–1979. *The Royal Society, London,* 15–18.
- 852 Sicali, S., M. Barbano, S. D’Amico, and R. Azzaro (2014). Characterization  
853 of seismicity at Mt. Etna volcano (Italy) by inter-event time distribution.  
854 *J. Volc. Geotherm. Res. 270,* 1–9.
- 855 Singh, S. and R. B. Herrmann (1983). Regionalization of Crustal Coda Q in  
856 the continental United States. *Journal of Geophysical Research 88(B1),*  
857 *527–538.*

- 858 Sketsiou, P., F. Napolitano, A. Zenonos, and L. De Siena (2020). New  
859 insights into seismic absorption imaging. *Physics of the Earth and Planetary  
860 Interiors* 298(<https://doi.org/10.1016/j.pepi.2019.106337>).
- 861 Snieder, R. (2004). Coda wave interferometry. *McGraw-Hill Yearbook of  
862 Science & Technology* 2004, 3.
- 863 Solaro, G., V. Acocella, S. Pepe, J. Ruch, M. Neri, , and E. Sansosti  
864 (2010). Anatomy of an unstable volcano from InSAR: multiple processes  
865 affecting flank instability at Mt. Etna, 1994–2008. *J. Geophys. Res.* 115,  
866 B10405(<https://doi.org/10.1029/2009JB000820>).
- 867 Tanguy, J., M. Condomines, and G. Kieer (1997). Evolution of Mount Etna  
868 magma: Constraints on the present feeding system and eruptive mecha-  
869 nism. *J. Volcanol. Geotherm. Res.* 75, 221–250.
- 870 Urlaub, M., F. Petersen, F. Gross, A. Bonforte, G. Puglisi, and  
871 F. Guglielmino (2018). Gravitational collapse of Mount Etna’s south-  
872 eastern flank. *Science Advances* 4(10).
- 873 Xie, J. and B. Mitchell (1990). A Back-Projection Method for Imaging Large-  
874 Scale Lateral Variations of Lg Coda Q with Application to Continental  
875 Africa. *Geophysical Journal International* 100(2), 161–181.
- 876 Zeng, Y., F. Su, and K. Aki (1991). Scattering wave energy propagation  
877 in a random isotropic scattering medium. Part 1. Theory. *Journal Of  
878 Geophysical Research-Solid Earth* 96, 607–619.
- 879 Zhang, T., C. Sens-Shofelder, and L. Margerin (2021). Sensitivity kernels

880 for static and dynamic tomography of scattering and absorbing media  
881 with elastic waves: a probabilistic approach. *Geophys. J. Int* (ggab048 (in  
882 press)).

## 883 **Appendix 1 - The approximate 3D weighting func-** 884 **tions**

885 In the approach used in the present paper,  $Q_{cj}$  is seen as a single measure  
886 of a repeated set of measures. The weighting functions in this approach give  
887 the probability that in the space point of given coordinates, the measure  
888 assumes effectively that value. The measure set thus produce for any pixel  
889  $j$ , a set of point values of Q-coda multiplied by their probability,  $\bar{q}_i w_{ij}$ . We  
890 consider their weighted average as the characteristic value of Q-coda in the  
891 specific point. In other words, we simply “project” the Q-coda measure, or  
892 “attribute” the measure to a space point of given coordinates weighting for  
893 the weighting functions. A similar approach has been applied for example  
894 by Mayor et al. (2016), Prudencio et al. (13 a), Prudencio et al. (2017).  
895 The standard deviation of the Q-coda “projected” into the 3D volume under  
896 study can be easily calculated pixel by pixel, as an estimate of the uncertainty  
897 associated with the Q-coda pixel values . The 3D weighting functions for  
898 Q-coda can be calculated as described in Del Pezzo and Ibañez (2020) and in  
899 the references therein. Here we report its polynomial approximation used in  
900 the present approach, slightly modified from the one described in Del Pezzo  
901 and Ibañez (2020) in the term which accounts for the distance dependence

902 (equation 7):

$$w(x, y, z, r, t_l, v) = \frac{f_1(x, y, z, r, t_l, v) + f_2(x, y, z, r, t_l, v)}{\text{Max}(f_1 + f_2)} \quad (4)$$

903 where

$$f_1(x, y, z, r, t_l, v) = \frac{1}{2\pi\sigma(r, t_l, v)^3} \exp\left(-\frac{d_1^2}{2\sigma(r, t_l, v)^2}\right) + \frac{1}{2\pi\sigma(r, t_l, v)^3} \exp\left(-\frac{d_2^2}{2\sigma(r, t_l, v)^2}\right) \quad (5)$$

$$f_2(x, y, z, r, t_l, v) = \frac{1}{6\pi\sigma(r, t_l, v)^3} \exp\left(-\frac{d_{1/2}^2}{2\sigma(r, t_l, v)^2}\right) \quad (6)$$

$$\sigma(x, y, z, x_s, y_s, z_s, x_r, y_r, t_l, v) = \frac{t_l v}{10} - \frac{r}{5} \quad (7)$$

$$r = \sqrt{(x_r - x_s)^2 + (y_r - y_s)^2 + (-z_s)^2}$$

$$d_1 = \sqrt{(x - x_s)^2 + (y - y_s)^2 + (z - z_s)^2}$$

$$d_2 = \sqrt{(x - x_r)^2 + (y - y_r)^2 + z^2}$$

$$d_{1/2} = \sqrt{\left(x - \frac{x_s + x_r}{2}\right)^2 + \left(y - \frac{y_s + y_r}{2}\right)^2 + \left(z - \frac{z_s}{2}\right)^2}$$

904  $d_1$ ,  $d_2$  and  $d_{1/2}$  represent respectively the distance between the space coor-  
 905 dinate and the source, between the space coordinate and the receiver and  
 906 between the space coordinate and the source-receiver midpoint.

## 907 Appendix 2 - Resolution and uncertainties

908 The Q-coda weighting functions (Del Pezzo and Ibañez, 2020) are here de-  
 909 noted as

$$w_{ij}(x_j, y_j, z_j, x_{ri}, y_{ri}, x_{si}, y_{si}, z_{si})$$

910  $w_{ij}$  represents the probability that, for the  $i$ -th source-receiver couple po-  
 911 sitioned respectively at  $\{x_{si}, y_{si}, z_{si}\}$  and  $\{x_{ri}, y_{ri}\}$ , the measured value of  
 912 Q-coda effectively corresponds to the true value at the space point with co-  
 913 ordinates  $x_j$ ,  $y_j$  and  $z_j$ . For an exhausting review see Del Pezzo and Ibañez  
 914 (2020).  $j$  is the index associated with the  $j$ -th pixel of generic coordinates  
 915  $\{x, y\}$ .  $i$  spans from 1 to  $N$  ( $N$  is the number of source-receiver couples in  
 916 the data set).  $j$  spans from 1 to  $M$  where  $M$  is the number of cells in which  
 917 the space has been divided (improperly called "pixels").  $\bar{q}_i$  is the measure  
 918 of  $Q_c$  for the  $i$ -th source-receiver pair;  $\bar{q}_j$  is the results for the  $j$ -th pixel.

919 The "back-projection" method yields

$$Q_{cj} = \frac{\sum_i \bar{q}_i w_{ij}}{\sum_i w_{ij}} \quad (8)$$

920 In this heuristic scheme,  $w_{ij}$  represents the un-normalized probability that  
 921 the  $i$ -th measure,  $\bar{q}_i$ , is associated with the  $j$ -th pixel.

922 Calling  $\sigma_i$  the standard deviation correspondent to the  $i$ -th measure,  $\bar{q}_i$

923 , and applying the ordinary error propagation equation to eq. (8) we obtain

$$\sigma_{Q_{cj}}^2 = \sum_i \left( \frac{\partial Q_{cj}}{\partial q_i} \right)^2 \sigma_i^2 = \frac{1}{(\sum_i w_{ij})^2} \sum_i w_{ij}^2 \sigma_i^2 \quad (9)$$

924 As can be immediately deduced, if  $w_{ij} = 1$  and  $\sigma_i = \sigma$  for every  $i$  and  
 925  $j$  ,  $\sigma_{q_j} = \frac{\sigma}{\sqrt{N}}$ , as for the simple arithmetical average. We assume that the  
 926 quantity proportional to the standard error inverse (normalized by  $\sigma$ ),  $\sigma/\sigma_{q_j}$ ,  
 927 represents a reasonable estimate of the resolution of the method. Thus, the  
 928 pixels showing smaller resolution are associated with higher errors and vice-  
 929 versa.

930 Resolution at the  $j - th$  pixel is thus given by

$$R_j = \sqrt{\frac{(\sum_i w_{ij})^2}{\sum_i w_{ij}^2}} \quad (10)$$

931 Equation (9) can be usefully used to estimate the standard deviation associ-  
 932 ated with the Q-coda estimated in the single pixel. In this procedure,  $\sigma_{Q_{cj}}$   
 933 may result apparently small even for small  $R_j$ , but this may be due to the  
 934 data scarcity in that j-th pixel, and the estimate may be strongly changed  
 935 by adding more data. On the contrary, the estimates of  $\sigma_{q_j}$  are relatively  
 936 stable in pixels characterized by high  $R_j$  .

937 We applied equation (9) to the present values.  $\sigma_i$  values were estimated  
 938 from the best fit of the coda envelopes to the Single-scattering model (Sato  
 939 et al., 2012). The values of standard deviations of  $Q_c$ ,  $\sigma_{Q_{cj}}$  , associated with  
 940 the any single  $j - th$  pixel, resulted to be in the interval between 2 and 20,  
 941 with means around  $\sigma_{q_j} = 10$ . This is the reason why in the plots of Figure 4  
 942 and Figure 6 we used an interval of 10.0 between adjacent isolines.